

# Fatty Alcohol-Based “Smart Windows” Driven by Photo-Thermal Materials Toward Thermal Management in Hot Regions and High Fire Safety

Wei Cai, Tianyang Cui, Liangyuan Qi, Junling Wang, Wei Wang, Chengfei Cao, Shuo Shi, Xin Hu, Mohammad Ziaur Rahman, Weiyi Xing,\* De-Yi Wang,\* and Bin Fei\*

In modern architecture, windows are increasingly employed as curtain wall structures, playing a critical approach in regulating indoor environments to reduce building energy consumption. Meanwhile, the demands for transparency and flame retardancy present significant challenges in guaranteeing people's privacy and safety. In response, a two-layer “smart window” is designed to achieve thermal management, privacy protection, and fire safety, through leveraging the photo-thermal effect of MXene nanosheets, the phase change characteristic of fatty alcohol, and the flame-retardant effect of tetrabromobisphenol A (TBBPA). In the daytime, MXene not only absorbs solar energy to mitigate its heating effect on indoor temperatures and achieve an average decrease of  $\approx 4.2$  °C but also facilitates the melting of fatty alcohol to provide optimal daylighting conditions (transmissivity of 65.0%). In the nighttime, the solidified fatty alcohol prevents light transmittance (modulation of 30.6%) and significantly enhances the light deviation to protect personal privacy. Besides, TBBPA dissolved in fatty alcohol effectively enhances the fire safety performance of “smart windows” without sacrificing the transparency. Most importantly, the manufacturing approach is extremely simple to present significant advantages compared to other “smart windows”, promoting its practical application in emerging buildings in terms of energy saving, privacy protection, and fire safety.

outer walls play crucial roles in exchanging indoor heat with the environment.<sup>[2]</sup> To reduce energy consumption in building cooling, research institutes and scholars worldwide are dedicated to developing daytime radiative cooling materials that can be applied to exterior walls. These materials reflect solar energy and radiate the building's heat outward.<sup>[2b,3]</sup> While numerous studies focus on the application of radiative cooling materials on building walls, the development of smart windows has received less attention and poses a greater challenge due to the requirement for transparency.<sup>[4]</sup>

Although there is less research on smart windows compared to daytime radiative cooling materials, various types of smart windows have been designed and fabricated to regulate indoor environments, including thermochromic, electrochromic, and photochromic windows.<sup>[5]</sup> Notably, vanadium dioxide (VO<sub>2</sub>), known for its reversible metal-to-insulator transition, has been synthesized to create polymer-based nanocomposites that reflect near-infrared

(NIR) light from solar illumination, serving as a representative thermochromic material.<sup>[6]</sup> For instance, VO<sub>2</sub> nanoparticles are spin-coated onto the surface of a poly(methyl methacrylate) (PMMA) spacer, using PMMA as a polymer binder to modulate transmittance.<sup>[6b]</sup> Due to its reflective properties in the NIR region, a solar transmission modulation of  $\approx 9.3\%$  is achieved,

## 1. Introduction

The indoor environment adjustments of buildings account for  $\approx 40\%$  of global energy consumption, encompassing ventilation, heating, and cooling.<sup>[1]</sup> Even worse, this figure is steadily rising due to the pursuit of higher living standards. Windows and

W. Cai, S. Shi, X. Hu, M. Z. Rahman, B. Fei  
School of Fashion and Textiles  
The Hong Kong Polytechnic University  
Kowloon, Hong Kong SAR 999077, P. R. China  
E-mail: [bin.fe@polyu.edu.hk](mailto:bin.fe@polyu.edu.hk)

W. Cai, D.-Y. Wang  
IMDEA Materials Institute  
C/Eric Kandel, 2, Getafe, Madrid 28906, Spain  
E-mail: [deyi.wang@imdea.org](mailto:deyi.wang@imdea.org)

T. Cui, L. Qi, W. Xing  
State Key Laboratory of Fire Science  
University of Science and Technology of China  
Hefei 230026, P. R. China  
E-mail: [xingwy@ustc.edu.cn](mailto:xingwy@ustc.edu.cn)

J. Wang  
Department of Architecture and Civil Engineering  
City University of Hong Kong  
Tat Chee Avenue, Kowloon, Hong Kong 999077, P. R. China

W. Wang, C. Cao  
School of Mechanical and Manufacturing Engineering  
University of New South Wales  
Sydney, NSW 2052, Australia

The ORCID identification number(s) for the author(s) of this article can be found under <https://doi.org/10.1002/smll.202501540>

© 2025 The Author(s). Small published by Wiley-VCH GmbH. This is an open access article under the terms of the [Creative Commons Attribution-NonCommercial-NoDerivs](https://creativecommons.org/licenses/by-nc-nd/4.0/) License, which permits use and distribution in any medium, provided the original work is properly cited, the use is non-commercial and no modifications or adaptations are made.

DOI: 10.1002/smll.202501540

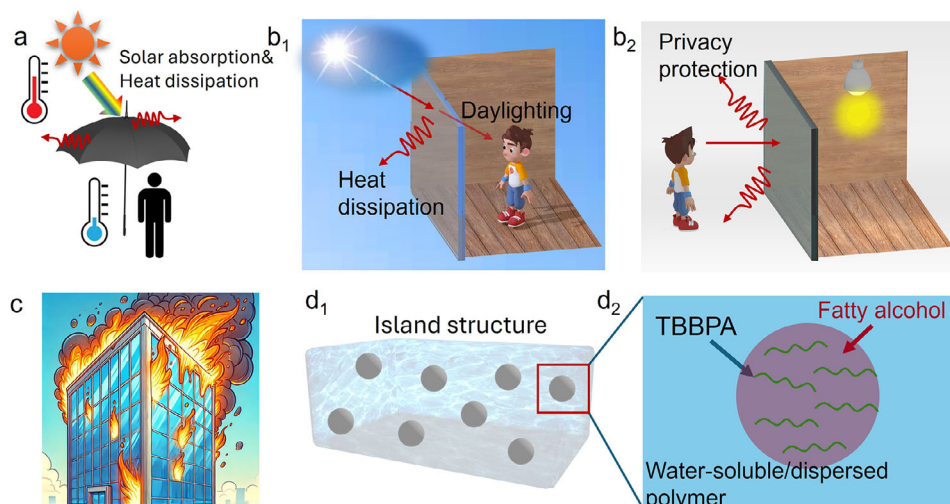


**Figure 1.** Design concept of smart window with thermal management, privacy protection, and fire safety. (a) Conventional design of sun umbrella, absorbing solar energy to decrease the bottom temperature; Working principle of smart window at daytime (b<sub>1</sub>) and nighttime (b<sub>2</sub>); (c) The vertical propagation of fire along glass curtain wall; (d<sub>1</sub> and d<sub>2</sub>) The dispersion state of fatty alcohol and TBBPA within WPU matrix.

reducing the NIR heating effect during hot seasons. Despite the significant potential of VO<sub>2</sub>-based smart windows to regulate room temperature, their transition temperature ( $\approx 68$  °C) between metal and insulator states is much higher than typical room or environmental temperatures and needs to be lowered through doping strategies.<sup>[7]</sup> By the Fe/Mg co-doping approach, a phase transition temperature  $\approx 38.2$  °C is realized by Jiang et al.<sup>[8]</sup> However, the preparation and application of VO<sub>2</sub> nanoparticles doped by other elements will significantly increase the commercial cost in the practical application, particularly due to the high-temperature calcination involved.<sup>[9]</sup>

In addition to vanadium dioxide, hydrogel-based thermochromic windows are also garnering wide attention from academic institutions and researchers. The thermochromic mechanism in hydrogels primarily stems from the structure transformation of polymer molecules, which causes the switch between hydrophilicity and hydrophobicity.<sup>[10]</sup> When the environment temperature exceeds a critical temperature, polymer molecules that are well dissolved in hydrogels become hydrophobic and aggregate together to form micelles, further blocking light transmission. Recent research on hydrogel-based thermochromic windows has focused on the design, functionalization, and modification of poly(N-isopropylacrylamide) (PNIPAM). For instance, Fu et al. introduce hydrophilic monomer N, N-dimethylacrylamide (DMAA) in the molecule structure of PNIPAM through the in situ free radical copolymerization, reducing the critical temperature to 32.5 from 43.5 °C.<sup>[10]</sup> This structural design achieves solar modulation of up to 88.84% and intrinsic transmittance of up to 91.30% across the full spectrum, resulting in energy savings of up to 4.30 J m<sup>-3</sup>, as confirmed by the *EnergyPlus* simulation.<sup>[10]</sup> However, the raw materials for synthesizing PNIPAM are expensive, hindering further commercial popularization. Meanwhile, uniformly injecting hydrogels between two sheets of glass with a large manufacturing scale is extremely challenging and poses a risk of leakage.

Here's a practical example the window used in automobile skylights usually employs a transparent black structure to ab-

sorb solar energy, thus decreasing the heating effect on the car's interior temperature. A similar phenomenon is observed with the sun umbrella (Figure 1a<sub>1</sub>). Unlike pure-white morphology in the daytime radiative cooling technology, the black characteristic helps avoid visual pollution associated with white surfaces.<sup>[11]</sup> However, incorporating black materials into windows can reduce transparency, affecting visual clarity. As an emerging 2D nanomaterial, MXene nanosheets have demonstrated a significant absorption effect in solar energy.<sup>[12]</sup> According to Sun et al., adding a small quantity of MXene nanosheets can still maintain a high transparency, evidenced by the high transmittance of 71.4% at 550 nm.<sup>[13]</sup> This means that coating MXene nanosheets onto glass surfaces can mitigate the solar heating effect in room temperature while preserving a desirable transparency. Interestingly, Silva et al. prepared a "smart" window by combining polyethylene glycol and chitin nanofibers, switching between transparent and vague states due to the phase change of polyethylene glycol in response to the environment temperature.<sup>[14]</sup> This window allows solar light penetration at 35 °C, while becoming opaque to protect privacy at 25 °C. However, the uniform and continuous dispersion of polyethylene glycol in the "smart" window poses a leakage risk.<sup>[15]</sup> As an alternative organic phase change material, fatty alcohol is insoluble in water and can form an island structure in water-soluble/dispersed polymer resin, addressing the typical leakage risk.<sup>[16]</sup> Besides, waterborne polyurethane (WPU) is a commercial cationic polymer (i.e., quaternary ammonium structure) that can be dispersed in water with a colloidal structure. Once dried, pure WPU is highly transparent. Therefore, incorporating fatty alcohol into WPU resin allows regulation of transparency and opacity through the melting and solid states of fatty alcohol, corresponding to transparent and white appearances, respectively. Under solar illumination, the photo-thermal MXene-based layer is capable of raising the temperature of the WPU/fatty alcohol composite to a liquid state, resulting in a transparent structure (Figure 1b<sub>1</sub>). Into the night, the fatty alcohol gradually cools to a solid state, creating an opaque appearance in the WPU/fatty

alcohol composite to further block the view from outside (Figure 1b<sub>2</sub>).

Recent research advancements usually neglect the fire hazard associated with smart windows that use polymer resin as base materials. For instance, PMMA is commonly used to incorporate VO<sub>2</sub> nanomaterials in the fabrication of smart windows.<sup>[17]</sup> As organic materials, typical polymers are highly flammable and can release a lot of heat and toxic gases. In addition, using polymer-based materials as the smart window can cause a vertical spread of fire along a wall (Figure 1c).<sup>[18]</sup> It has been found that bisphenol A can selectively dissolve in liquid fatty alcohol.<sup>[19]</sup> Tetrabromobisphenol-A (TBBPA), a commercial flame retardant with a structure similar to bisphenol A, may also dissolve in fatty alcohol. Although the flame-retardant mechanism of TBBPA can produce more smoke particles, outdoor conditions can effectively reduce the risk posed by these particles.<sup>[20]</sup> Meanwhile, on 10 December 2024, the European Union announced the termination of the legislative proposal to include tetrabromobisphenol A in the list of restricted substances of the RoHS Directive (2011/65/EU) with immediate effect. Herein, by leveraging the diverse dispersion properties in the water, TBBPA and fatty alcohol will together form an island structure within a water-soluble/dispersed polymer.

Herein, we aim to reduce energy consumption, ensure privacy, and enhance fire safety by utilizing the photo-thermal effect of MXene nanosheets, the phase change properties of fatty alcohol, and the flame-retardant capabilities of TBBPA. We have developed a smart, self-adaptive composite film that functions as a “smart window”, providing transparency during the day and light shielding at night (Figure 1b). Due to the photo-thermal effect of MXene, the fatty alcohol melts to meet the refractive index with a waterborne polyurethane (WPU) matrix, allowing for transparency during the day (Figure 1b<sub>1</sub>). Meanwhile, MXene nanosheets further absorb the solar energy, mitigating its heating effect on indoor temperatures. At night, the cooled and solidified fatty alcohol blocks light transmission and enhances light diffusion to protect privacy (Figure 1b<sub>2</sub>). Furthermore, the flame-retardant TBBPA, dissolved in fatty alcohol, addresses the issue of vertical fire propagation in high-rise buildings without affecting transparency. Most importantly, this work presents an extremely simple method for preparing a smart, self-adaptive composite film, advancing the development of thermal management materials to reduce building energy consumption.

## 2. Results and Discussion

### 2.1. The Synthesis of WPU/Fatty Alcohol

Herein, we present a two-layer “smart windows” designed to achieve thermal management, privacy protection, and fire safety, by leveraging the photo-thermal effect of MXene, phase change properties of fatty alcohol, and flame-retardant capabilities of tetrabromobisphenol A (TBBPA). The photo-thermal conversion effect of MXene nanosheets allows the phase change process of n-hexadecanol to be easily regulated by solar intensity, enabling the transition between white and transparent states. Given the high temperature generated by the photo-thermal conversion of MXene nanosheets, a high phase change temperature

is essential for practical application, preventing the melting behavior of fatty alcohols at low solar intensities. Among fatty alcohols, n-hexadecanol with a phase change temperature near 50 °C, remains solid, making it an ideal choice for exploring the transparency and opacity-switching behavior of this smart window design. First, n-hexadecanol (C<sub>16</sub>-OH) and WPU are physically mixed at room temperature in varying mass ratios and gradually heated to 80 °C. As n-hexadecanol is non-polar and insoluble in water, it forms oil droplets within the WPU solution during heating and stirring. Meanwhile, the blending temperature of 80 °C disrupts the colloidal dispersion of the WPU solution, precipitating in the mixture.<sup>[21]</sup> It is hypothesized that the WPU molecule will assemble onto the surface of n-hexadecanol droplets, gradually losing fluidity (Figure 2a). After the uniform blend, the WPU/C<sub>16</sub>-OH composite becomes sufficiently viscous to be applied onto the surface using the blade method. Composites with 10, 20, 30, 40, and 50 wt.% n-hexadecanol in the WPU matrix are designated as WPU-1, WPU-2, WPU-3, WPU-4, and WPU-5, respectively. The prepared WPU/C<sub>16</sub>-OH composite films are then adhered onto the top of a patterned surface (Figure 2b). It was found that, even though the addition of 30 and 50 wt.% n-hexadecanol in WPU (WPU-3 and WPU-5) obviously decreases the transparency, the underlying pattern remains visible. When placed 2 cm above the pattern, WPU-5 gradually and completely obscures the pattern as it cools from 60 °C to room temperature (≈21 °C), due to its high haze value (Figure 2c; Figure S1, Supporting Information).<sup>[22]</sup> When heated to 60 °C, pure n-hexadecanol quickly melts and spreads (Figure 2d; Figure S2, Supporting Information). In contrast, the composite film becomes transparent while maintaining its structure (Figure 2d<sub>1</sub>). Upon cooling, both the composite film and pure n-hexadecanol revert to a non-transparent state (Figure 2d<sub>2</sub>; Figure S3, Supporting Information). Throughout the heating and cooling process, the leakage phenomenon isn't presented for this composite film, due to the packaging effect of WPU.<sup>[23]</sup> Based on the above phenomenon, the switch function between non-transparent and transparent of composite film is attributed to the phase change behavior of n-hexadecanol.

In addition, the effect of varying the amount of n-hexadecanol in the transmittance of the WPU composite is also examined (Figure 2e). As the proportion of n-hexadecanol increases, the transmittance of the WPU composite films decreases at room temperature. Even though the transmittance of WPU-5 remains above 40% in the solar wavelength range, the scattering effect of n-hexadecanol crystal successfully alters the angle of the incident light, resulting in a high haze value, as confirmed by Figure 2c. The transition between transparent and opaque states is achieved through the phase change of fatty alcohol. This means that different fatty alcohols and their mixture can provide different phase-change temperatures. In addition to pure n-hexadecanol, laurinol, and n-decanol, laurinol is mixed respectively with n-hexadecanol and n-decanol with a mass ratio of 1:1. Their switch temperatures, ranging from 0 to 50 °C, are revealed by the differential scanning calorimetry (DSC) curves, meeting the requirement in different environments and regions (Figure 2f). It is observed that the mixtures of fatty alcohols exhibit lower phase-change temperatures compared to individual fatty alcohols.

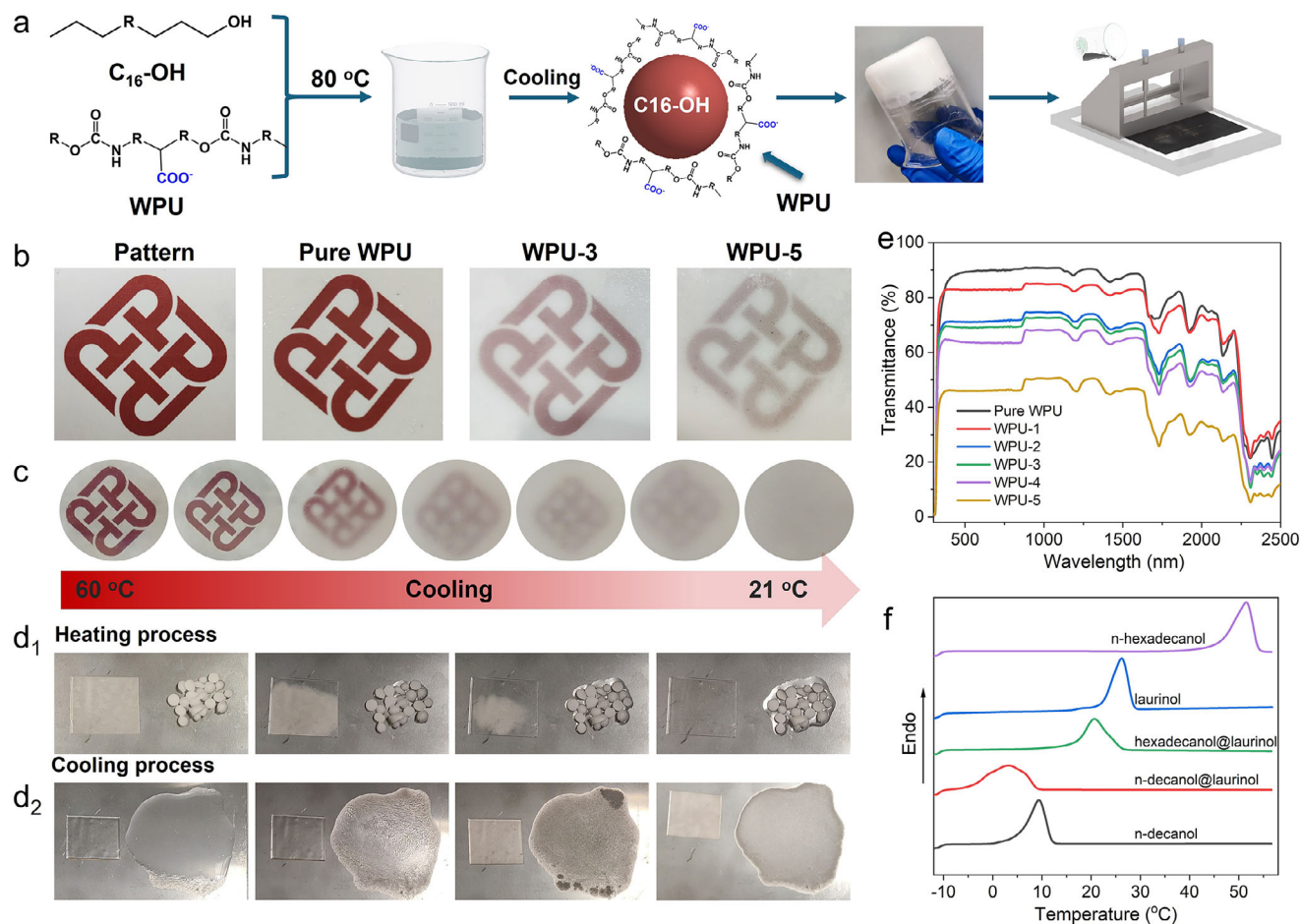


**Figure 2.** The exploratory result of WPU/fatty alcohol composite film. (a) Schematic for the preparation process of WPU/C<sub>16</sub>-OH composite film. (b) The transparency of WPU/C<sub>16</sub>-OH composite films with different amounts of C<sub>16</sub>-OH, attached closely to the pattern. (c) Transparency change of WPU-5 during the cooling process, setting a 2 cm distance to the pattern. The transparency and structure change of WPU-5 and C<sub>16</sub>-OH during heating (d<sub>1</sub>) and cooling process (d<sub>2</sub>). (e) The transmittance spectra for WPU/C<sub>16</sub>-OH composite with different amounts. (f) DSC curves of n-hexadecanol, laurinol, n-hexadecanol@n-decanol (mass ratio of 1:1), and laurinol@n-decanol (mass ratio of 1:1), confirming the adjustable switch temperature.

## 2.2. The Synthesis of WPU/MXene/C<sub>16</sub>-OH@TBBPA

Based on the above result, we further design the “smart windows”, using MXene as photo-thermal materials and TBBPA as flame retardants. As presented by Figure S4 (Supporting Information), TBBPA does not dissolve in hot water of 60 °C but dissolves rapidly in melting n-hexadecanol. Due to the structural similarity among fatty alcohols, TBBPA is likely soluble in other fatty alcohols such as laurinol and n-decanol. C<sub>16</sub>-OH, TBBPA, and WPU are mixed at 80 °C and then cool to room temperature (Figure 3a<sub>1</sub>). The mixed solution is bladed onto the surface of polytetrafluoroethylene (PTFE) mold and dried at room temperature to form the bottom structure (WPU/C<sub>16</sub>-OH@TBBPA). The top structure consists of a WPU/MXene composite coating, with MXene prepared according to our previous work.<sup>[24]</sup> The transmission electron microscope (TEM) image and X-Ray Diffraction (XRD) spectrum of MXene nanosheets are respectively demonstrated in Figures S5 and S6 (Supporting Information), with authorized copyrights.<sup>[24]</sup> MXene nanosheets are directly added to the WPU solution and sonicated to achieve a well-

dispersion state (Figure 3a<sub>2</sub>). The MXene content is kept at 0.2 wt.% to ensure sufficient transparency. Similarly, WPU/MXene composite film is prepared by the blading coating method on a PTFE mold. The two films are then pressed together to form a double-layer composite film (Figure 3b). The fracture surface of the two-double composite film is observed by scanning electron microscope (SEM) image, revealing a distinct boundary line (marked by red line, Figure 3c<sub>1</sub>). The left structure, WPU/C<sub>16</sub>-OH@TBBPA, exhibits a special porous structure attributed to the fatty alcohol (Figure 3c<sub>2</sub>,c<sub>3</sub>). The right structure, WPU/MXene composite coating, displays a smooth and flat morphology (Figure 3c<sub>4</sub>). As observed from Figure 3c<sub>3</sub>, the pores are discontinuous and surrounded by a resin matrix, forming an island structure for n-hexadecanol. In addition, compared to other literature reporting WPU/MXene composites, the smooth fracture surface structure is attributed to the low addition amount of MXene nanosheets, which is not capable of significantly enhancing the interfacial interaction.<sup>[25]</sup> Through SEM EDS spectra, Br and Ti elements is successfully detected in WPU/C<sub>16</sub>-OH@TBBPA and WPU/MXene, respectively (Figure 3d<sub>1</sub>,d<sub>2</sub>).

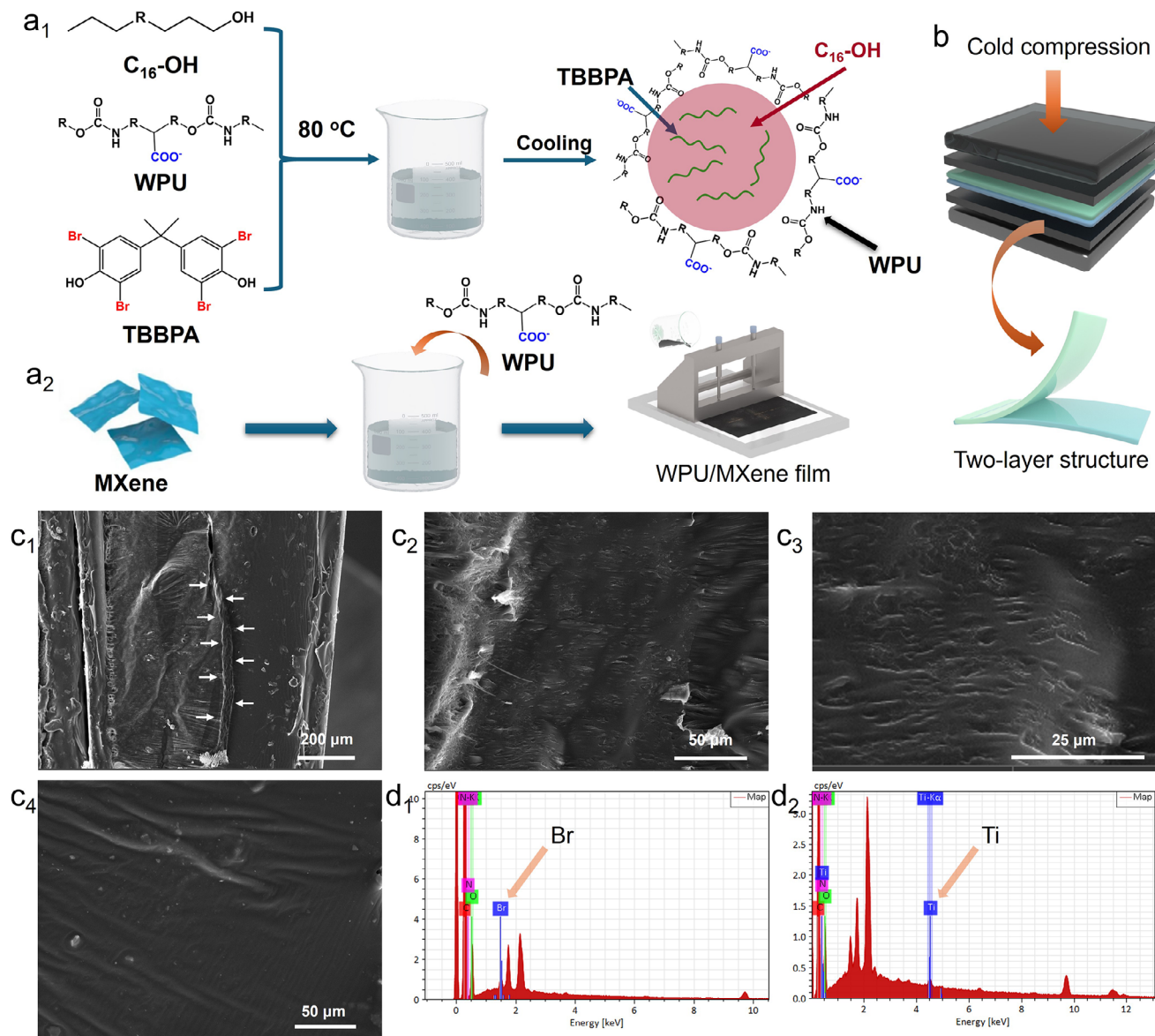


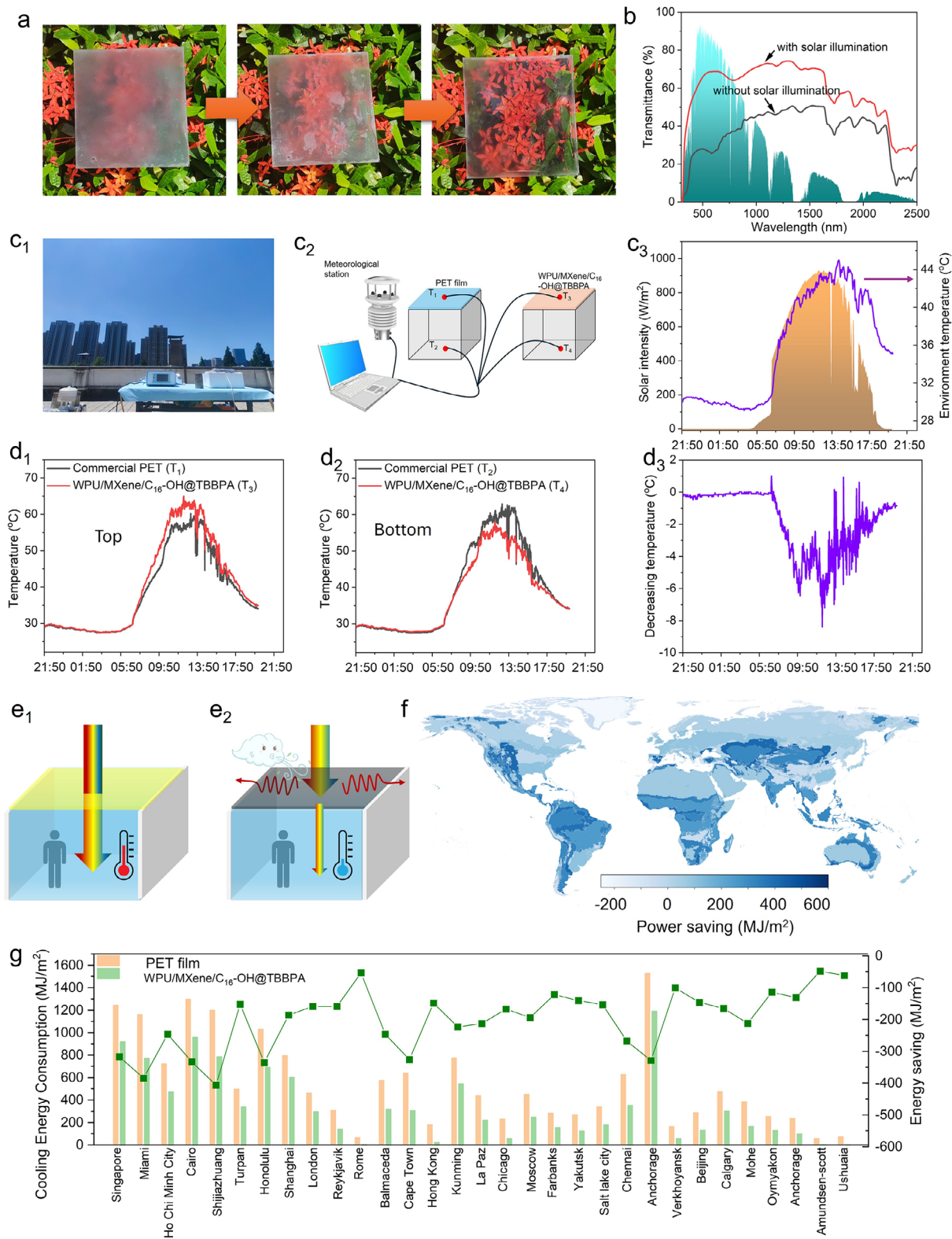
**Figure 3.** The preparation and structure characterization of WPU/MXene/C<sub>16</sub>-OH@TBBPA. The preparation schematic of WPU/C<sub>16</sub>-OH@TBBPA (a<sub>1</sub>) and WPU/MXene (a<sub>2</sub>). (b) Schematic for the formation of a two-layer composite layer by the cold compression. SEM images of the fracture surface of WPU/MXene/C<sub>16</sub>-OH@TBBPA film (c<sub>1</sub>), while left and right regions are corresponding to WPU/C<sub>16</sub>-OH@TBBPA and WPU/MXene films, respectively. (c<sub>2</sub> and c<sub>3</sub>) SEM images of fracture surface of WPU/C<sub>16</sub>-OH@TBBPA film in different resolutions. (c<sub>4</sub>) SEM image of the fracture surface of WPU/MXene film. SEM-EDS spectra of WPU/C<sub>16</sub>-OH@TBBPA (d<sub>1</sub>) and WPU/MXene films (d<sub>2</sub>).

Although TBBPA shows selective solubility in n-hexadecanol, the island dispersion of the Br element is not visible in the SEM Mapping spectrum (Figure S7, Supporting Information), possibly due to the low element ratio. The mechanical performance of WPU/MXene/C<sub>16</sub>-OH@TBBPA is further evaluated through the tensile test (Figure S8, Supporting Information). It is found that the break strength and elongation at break of WPU/MXene/C<sub>16</sub>-OH@TBBPA are decreased to 14.5 MPa and 340%, presenting decreases of 28.2% and 37.0% compared to those of pure WPU (20.2 MPa and 540%). However, these values still satisfy the practical application for this double-layer composite film. Based on the above analyses, the double-layer composite film is success-

fully prepared by cold pressing of WPU/C<sub>16</sub>-OH@TBBPA and WPU/MXene composite films together.

### 2.3. Thermal Management Performance

As reported previously, MXene nanosheets exhibit a superior photo-thermal conversion function, effectively converting solar energy into heat.<sup>[13]</sup> Consequently, WPU/MXene composite film is expected to absorb solar energy and heat the WPU/C<sub>16</sub>-OH@TBBPA layer, thus achieving high transparency. As shown in Figures 4a and S9 (Supporting Information), when the



double-layer composite film is placed over flowering shrubs and exposed to solar illumination, it gradually transitions from opaque to transparent, allowing the flowers beneath to be clearly seen. This smart, self-adaptive feature enables the composite film to either allow light to pass through or block it, depending on solar intensity. Based on Figure 2d, the switch between transparent and vague is attributed to the thermal melting of n-hexadecanol, with the photo-thermal conversion effect of MXene nanosheets. Under illumination of  $1.0 \text{ kW m}^{-2}$ , the surface temperature of WPU/MXene/C<sub>16</sub>-OH@TBBPA is recorded by the thermocouple and infrared thermal images. As shown by Figure S10 (Supporting Information), the surface temperature rapidly increases to  $\approx 70 \text{ }^\circ\text{C}$  within 5 min, which is further maintained near 50 min. When the simulated solar illumination is removed, the surface temperature presents a sudden decreasing trend, indicating that the high temperature is from the photo-thermal conversion effect. The corresponding infrared thermal images are also presented in Figure S11 (Supporting Information), indicating a rapid heating process. In addition, n-hexadecanol is dispersed within the WPU matrix with an island structure. The packaging effect of WPU resin effectively suppresses the leakage behavior of n-hexadecanol. After being placed in the outdoor environment for 30 days, the switch between transparent and vague is still presented, confirming the desirable durability (Figure S12, Supporting Information). The transmittance of double-layer composite film at different states is studied by the UV-vis-NIR spectrum (Figure 4b). According to previous work, the overall transmittance can be calculated by formula 1), indicating that the transmittance is increased to 65.0% from 34.4%.<sup>[19]</sup> The transmittance of up to 65.0% indicates a well lighting performance.<sup>[26]</sup> In addition, the IR emissivity in the atmospheric transmission window of double-layer composite film in opaque states is also examined. Based on formula 2), the emissivity of the two-layer composite film is  $\approx 86.3\%$  (Figure S13, Supporting Information).

The open-air experiment was conducted to investigate the thermal management performance in Hefei, China ( $31^\circ 49' 14'' \text{N}$  and  $117^\circ 13' 38'' \text{E}$ ). The experiment took place from 21:50 20-July-2024 to 21:00 21-July-2024, under sunny and cloudless weather (Figure 4c<sub>1</sub>). Similar to previous work, the experimental setup included thermocouples, a meteorological station, and hollow polystyrene (PS) foam (Figure 4c<sub>2</sub>).<sup>[19]</sup> The hollow PS foam, covered with either WPU/MXene/C<sub>16</sub>-OH@TBBPA or commercial polyethylene terephthalate (PET), is wrapped in aluminum paper to minimize environmental influences. The thermocouples were attached to the top and bottom of hollow PS foam to record temperatures. The well weather condition provides a solar intensity of up to  $924 \text{ W m}^{-2}$ , resulting in an ambient temperature of near  $44 \text{ }^\circ\text{C}$  (Figure 4c<sub>3</sub>). In nighttime, similar temperatures were recorded at the top and bottom locations for both commercial PET and WPU/MXene/C<sub>16</sub>-OH@TBBPA, likely due to the low IR emissivity of composite film (Figure S13, Sup-

porting Information). Near 07:50, temperatures in the top location for both commercial PET and composite film designed are rapidly increased, due to the solar illumination (Figure 4d<sub>1</sub>). Meanwhile, the temperature of WPU/MXene/C<sub>16</sub>-OH@TBBPA composite film is significantly higher than that of commercial PET, clearly attributed to the photo-thermal conversion effect. From 10:50 to 12:50, the average temperature increase between commercial PET and WPU/MXene/C<sub>16</sub>-OH@TBBPA composite film is  $\approx 4.87 \text{ }^\circ\text{C}$ . Temperatures recorded at the bottom of hollow PS foam present different characteristics (Figure 4d<sub>2</sub>). First, the noticeable difference in bottom temperatures began at 08:50 and became a significant difference after 09:50. However, this corresponding phenomenon appeared earlier in the top temperature, due to the top films shielding solar energy. Second, the photo-thermal effect of WPU/MXene/C<sub>16</sub>-OH@TBBPA significantly reduced the solar energy reaching the bottom of the hollow PS foam, resulting in a much lower bottom temperature. From 09:50 to 15:50, the average temperature decrease between commercial PET and WPU/MXene/C<sub>16</sub>-OH@TBBPA composite film was  $-4.2 \text{ }^\circ\text{C}$  (Figure 4d<sub>3</sub>). As the sun set, temperatures at both the top and bottom locations gradually decreased. The cooling mechanism of WPU/MXene/C<sub>16</sub>-OH@TBBPA is demonstrated by Figure 4e. When used as the roof material, the transparent PET cannot block the sunlight, allowing solar radiation to directly heat the bottom region (Figure 4e<sub>1</sub>). In contrast, WPU/MXene/C<sub>16</sub>-OH@TBBPA is capable of exhibiting a solar thermal conversion effect to suppress the direct illumination of solar radiation to the bottom region. Meanwhile, the heat generated by the solar thermal conversion effect of WPU/MXene/C<sub>16</sub>-OH@TBBPA will be directly dissipated by the external environment, particularly through wind action (Figure 4e<sub>2</sub>).

Due to the combination of the phase change function of n-hexadecanol and the photo-thermal conversion capabilities of MXene nanosheets, this composite film is designed to absorb solar energy, thereby reducing indoor temperatures and providing excellent transparency during the day, while also protecting privacy at night. In addition, the simulation of energy consumption using WPU/MXene/C<sub>16</sub>-OH@TBBPA was conducted by the *EnergyPlus* software, compared to commercial PET film. Detailed parameters are demonstrated in the experimental part. Meanwhile, as confirmed by Figure 2f, the switch temperature can be easily adjusted. Consequently, in this simulation,  $26 \text{ }^\circ\text{C}$  was selected as the switch temperature. Above  $26 \text{ }^\circ\text{C}$ , WPU/MXene/C<sub>16</sub>-OH@TBBPA is in a transparent state, while below  $26 \text{ }^\circ\text{C}$ , it becomes opaque. The heating and cooling modes correspond to 21 and  $26 \text{ }^\circ\text{C}$ , respectively. Importantly, the simulation focuses on window structures rather than wall structures, which is a significant distinction in *EnergyPlus* software. As presented by the energy saving mapping, the employment of WPU/MXene/C<sub>16</sub>-OH@TBBPA can effectively decrease the total building energy consumption in hot climate regions, including tropical rainy,

**Figure 4.** The thermal management performance of WPU/MXene/C<sub>16</sub>-OH@TBBPA. (a) The switch process from blurry to transparent under solar illumination; (b) Transmittance spectra with/without solar illumination; (c<sub>1</sub>) Digital picture for the field test of thermal management performance; (c<sub>2</sub>) Schematic for the home-made configuration for evaluating thermal management performance; (c<sub>3</sub>) The solar intensity and environment temperature during the field test; (d<sub>1</sub> and d<sub>2</sub>) Top and bottom temperatures of hollow PS foam using commercial PET and WPU/MXene/C<sub>16</sub>-OH@TBBPA as glass roof; (d<sub>3</sub>) Decrease value of two bottom temperatures; (e<sub>1</sub> and e<sub>2</sub>) Cooling mechanism brought by WPU/MXene/C<sub>16</sub>-OH@TBBPA; (f) Energy saving performance on a worldwide scale considering the energy consumed by cooling and heating systems, using Koppen's climatic province; (g) Energy saving performance on the representative climate city in cooling mode.

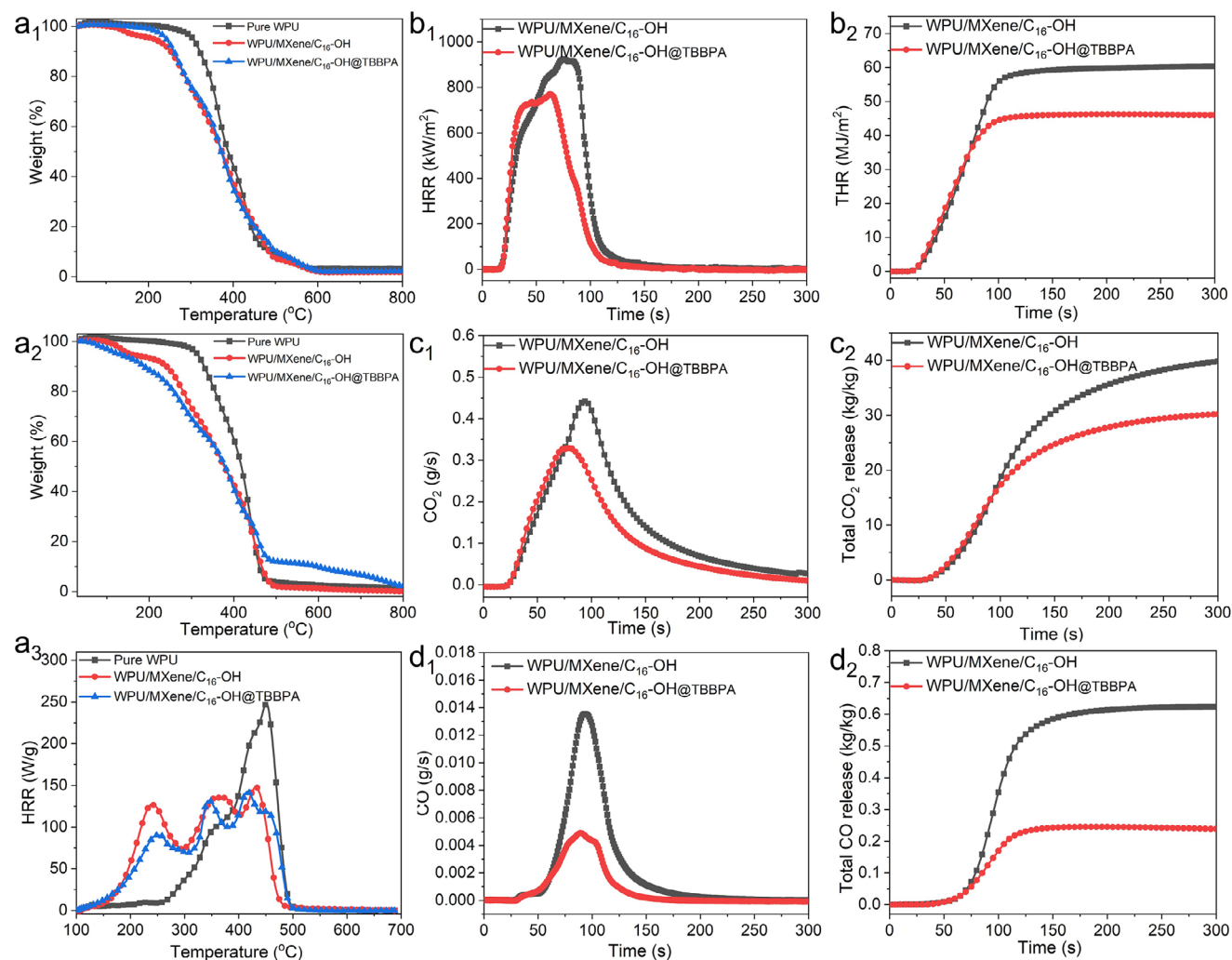


**Figure 5.** Fire safety performance investigation. Thermal stability performance of pure WPU and composite films designed at air ( $a_1$ ) and nitrogen ( $a_2$ ) atmospheres; ( $a_3$ ) MCC curves of pure WPU and composite films designed; The curves of heat release rate ( $b_1$ ), total heat release ( $b_2$ ), CO release rate ( $c_1$ ), total CO release ( $c_2$ ), CO release rate ( $d_1$ ), and total CO release ( $d_2$ ) of WPU/MXene/ $C_{16}$ -OH and WPU/MXene/ $C_{16}$ -OH@TBBPA.

tropical monsoon, tropical savanna, semi-arid steppe, and so on (Figure 4f). However, in some cold climatic regions, the employment of WPU/MXene/ $C_{16}$ -OH@TBBPA will further increase energy consumption. This outcome is attributed to the simultaneous consideration of heating and cooling modes. The total, cooling, and heating energy consumption in representative cities are respectively discussed in Figure 4g and Figures S14, and S15 (Supporting Information). For both cooling and heating modes, the largest energy saving is observed in Shijiazhuang city, while the largest energy consumption increase is shown in Amundsen-scott station. When considering only the cooling mode, the application of WPU/MXene/ $C_{16}$ -OH@TBBPA is able to decrease building energy consumption all over the world (up to  $406 \text{ MJ m}^{-2}$ ) (Figure 4f). However, the contrary result is presented when only considering the heating mode, increasing the energy consumption of all cities (Figure S15, Supporting Information). Therefore, this designed WPU/MXene/ $C_{16}$ -OH@TBBPA is suitable for hot cities and regions that primarily require cooling or have less reliance on heating.

#### 2.4. Fire Safety Evaluation and its Mechanism

The “smart windows” were prepared mainly by flammable WPU resin and fatty alcohol, which will release a lot of heat, smoke particles, and toxic gases during combustion.<sup>[27]</sup> In consideration of the practical application, it is very crucial to further investigate the fire hazard of WPU/MXene/ $C_{16}$ -OH@TBBPA. As presented in thermogravimetry analysis (TGA) results (Figure 5 $a_1, a_2$ ; Table S1, Supporting Information), compared to pure WPU, adding both n-hexadecanol and MXene will decrease the temperature corresponding to 5 wt.% mass loss of composite film whether air or nitrogen atmospheres, regarded as initial thermal decomposition temperature. This phenomenon is attributed to the short molecule chain of n-hexadecanol, resulting in a low thermal decomposition temperature.<sup>[28]</sup> There is no doubt that adding n-hexadecanol to the WPU matrix will significantly increase the fire hazard. Although flame-retardant MXene was also introduced, its addition amount is much lower than n-hexadecanol and cannot present an effective flame-retardant effect. It is interesting that

incorporating TBBPA to WPU/MXene/C<sub>16</sub>-OH only enhances its thermal stability under a nitrogen atmosphere, causing more residue from 450 °C to 800 °C (Figure 5a<sub>2</sub>). Micro calorimeter combustion test (MCC) was also conducted to analyze the thermal decomposition behavior (Figure 5a<sub>3</sub>; Figure S16, Supporting Information). In the MCC test, the samples are first pyrolyzed under a nitrogen atmosphere to release the flammable products which are then burned to produce the corresponding heat. It is reasonable to observe two heat release peaks in pure WPU, similar with the TGA curves. The peak of heat release rate (PHRR) and total heat release (THR) of pure WPU are up to 247 W g<sup>-1</sup> and 26.7 kJ g<sup>-1</sup>. Even though the addition of MXene and n-hexadecanol decreases the PHRR of WPU/MXene/C<sub>16</sub>-OH near 450 °C, its THR is significantly increased to 31.0 kJ g<sup>-1</sup>. In fact, the decrease in PHRR of WPU/MXene/C<sub>16</sub>-OH is attributed to less mass ratio for WPU, and more heat is released at lower temperatures near 250 °C due to the weak thermal stability of n-hexadecanol.<sup>[29]</sup> By releasing Br free radicals, the incorporation of TBBPA in WPU/MXene/C<sub>16</sub>-OH@TBBPA is able to play a gaseous flame-retardant effect to decrease the PHRR and THR, compared to WPU/MXene/C<sub>16</sub>-OH.<sup>[30]</sup>

The cone calorimeter test was further employed to assess the fire hazard of the WPU/MXene/C<sub>16</sub>-OH@TBBPA composite. The primary components of the composite film, WPU and n-hexadecanol, are the main contributors to fire hazard, rather than pure WPU. Meanwhile, the additional amount of MXene is low to 0.2 wt.%, which does not provide a significant flame-retardant effect. Therefore, we focused on comparing the combustion behavior of WPU/MXene/C<sub>16</sub>-OH and WPU/MXene/C<sub>16</sub>-OH@TBBPA. When exposed to a heat flux of 35 kW m<sup>-2</sup>, both composite films ignited rapidly in less than 10 s due to their low thermal stability. The PHRR values of WPU/MXene/C<sub>16</sub>-OH and WPU/MXene/C<sub>16</sub>-OH@TBBPA are 929 and 776 kW m<sup>2</sup>, respectively (Figure 5b<sub>1</sub>; Table S2, Supporting Information). The decrease of 16.5% in PHRR is attributed to the incorporation of 2 wt.% TBBPA. The time corresponding to the decrease in HRR is different. For WPU/MXene/C<sub>16</sub>-OH, the HRR begins to decrease rapidly and reaches zero ≈89 s. In contrast, the time corresponding to a decrease in HRR of WPU/MXene/C<sub>16</sub>-OH@TBBPA is obviously earlier than that of WPU/MXene/C<sub>16</sub>-OH, ≈64 s. The declining tendency in HRR indicates the suppressed or extinguished combustion behavior.<sup>[31]</sup> The distinctly different slopes suggest that the reduction in HRR after 64 s is due to the combustion suppression effect of TBBPA. As a result, the total heat release (THR) for WPU/MXene/C<sub>16</sub>-OH@TBBPA is reduced from 60.5 to 46.0 MJ m<sup>-2</sup> (Figure 5b<sub>2</sub>), representing a decrease of nearly 23.3% with the addition of 2 wt.% TBBPA.

In addition, the release behavior of CO<sub>2</sub> and CO was also measured using the cone calorimeter test. CO<sub>2</sub> is the primary gaseous product during polymer combustion, and its release behavior typically mirrors the heat release rate. Consequently, the CO<sub>2</sub> release behavior exhibits similar patterns to the HRR curves, including the timing of peak values and declining trends. The peak values of CO<sub>2</sub> release rate in WPU/MXene/C<sub>16</sub>-OH and WPU/MXene/C<sub>16</sub>-OH@TBBPA are 0.44 and 0.33 g s<sup>-1</sup>, respectively (Figure 5c<sub>1</sub>). Meanwhile, the total CO<sub>2</sub> release of WPU/MXene/C<sub>16</sub>-OH@TBBPA is decreased to 30.4 from 40.0 kg kg<sup>-1</sup> (WPU/MXene/C<sub>16</sub>-OH) (Figure 5c<sub>2</sub>). A more pro-

nounced reduction is observed in CO release. The CO release rate for WPU/MXene/C<sub>16</sub>-OH@TBBPA significantly decreased to 0.005 from 0.014 g s<sup>-1</sup> (WPU/MXene/C<sub>16</sub>-OH), with a decreasing percentage of 64.3% (Figure 5d<sub>1</sub>). Furthermore, the total CO release is also reduced by nearly 61.7% (Figure 5d<sub>2</sub>). Compared to the reductions in heat and CO<sub>2</sub>, the reductions in release rate and total release of CO are much more significant, indicating lower toxicity in terms of CO production.

## 2.5. Gaseous Flame-Retardant Mechanism

Due to the weak char-forming ability of the WPU matrix and a fatty alcohol, the char residue of WPU/MXene/C<sub>16</sub>-OH@TBBPA after the cone calorimeter test is minimal (Figure 6a).<sup>[32]</sup> Although the condensed-phase flame-retardant function of MXene nanosheets has been confirmed, its effectiveness is limited by the low addition amount.<sup>[33]</sup> In addition, TBBPA is a typical gaseous flame retardant.<sup>[30]</sup> Therefore, we focus on the gaseous flame-retardant mechanism and use Thermogravimetric analysis-Fourier transform infrared spectroscopy (TG-IR) to analyze the pyrolysis products. Figure 6b presents the 3D and top views of TG-IR spectra. Due to the varying test masses, the signal intensity of the same characteristic peaks cannot be directly compared across different samples. However, the relative intensity of different peaks within a single sample can be contrasted. The strongest signal intensity in pure WPU appears near 20 min and 2932 cm<sup>-1</sup> (Figure 6b<sub>1</sub>). According to TGA and MCC results, the time corresponding to the strongest signal intensity in WPU/MXene/C<sub>16</sub>-OH and WPU/MXene/C<sub>16</sub>-OH@TBBPA shifts to 10 min (Figure 6d<sub>2</sub>; Figure S17, Supporting Information). The Fourier Transform Infrared Spectroscopy (FTIR) spectra at the point of strongest signal are shown in Figure 6c. Clearly, the main pyrolysis products differ among pure WPU, WPU/MXene/C<sub>16</sub>-OH, and WPU/MXene/C<sub>16</sub>-OH@TBBPA. The pyrolysis products of pure WPU resin mainly include hydrocarbons (2950 m<sup>-1</sup>), carbonyl (1740 cm<sup>-1</sup>), aromatic compounds (1460 cm<sup>-1</sup>) and ether (1100 cm<sup>-1</sup>).<sup>[34]</sup> In contrast, the composite films mainly exhibit a prominent peak at 2930 cm<sup>-1</sup>, with no observable carbonyl peak, despite the WPU mass ratio being close to 75 wt.%, indicating a significant carbonyl presence.<sup>[35]</sup> This unusual phenomenon may be due to the incorporation of fatty alcohol altering the thermal decomposition behavior of WPU molecules, resulting in mutual interaction rather than independent decomposition.<sup>[35]</sup> The presence of numerous carbon radicals from decomposed fatty alcohol likely converts carbonyl structures into ether compounds.<sup>[36]</sup> Meanwhile, the remaining weak intensity of ether compounds at 1100 cm<sup>-1</sup> is attributed to the relatively stronger signal intensity of hydrocarbons. After normalizing by the test mass, the peak intensity of pyrolysis products of WPU/MXene/C<sub>16</sub>-OH and WPU/MXene/C<sub>16</sub>-OH@TBBPA can be further compared (Figure 6d<sub>1</sub>-d<sub>3</sub>; Figure S14, Supporting Information).<sup>[37]</sup> TGA results confirm that the pyrolysis products near 10 and 20 min originate from n-hexadecanol and WPU, respectively (Figure 5a<sub>1</sub>). The intensity of characteristic peaks located at 2932 and 2863 cm<sup>-1</sup> near 10 min, corresponding to hydrocarbons released from n-hexadecanol, are effectively decreased. However, peak intensities of 1461 and 1049 cm<sup>-1</sup> near 10 min are not effectively

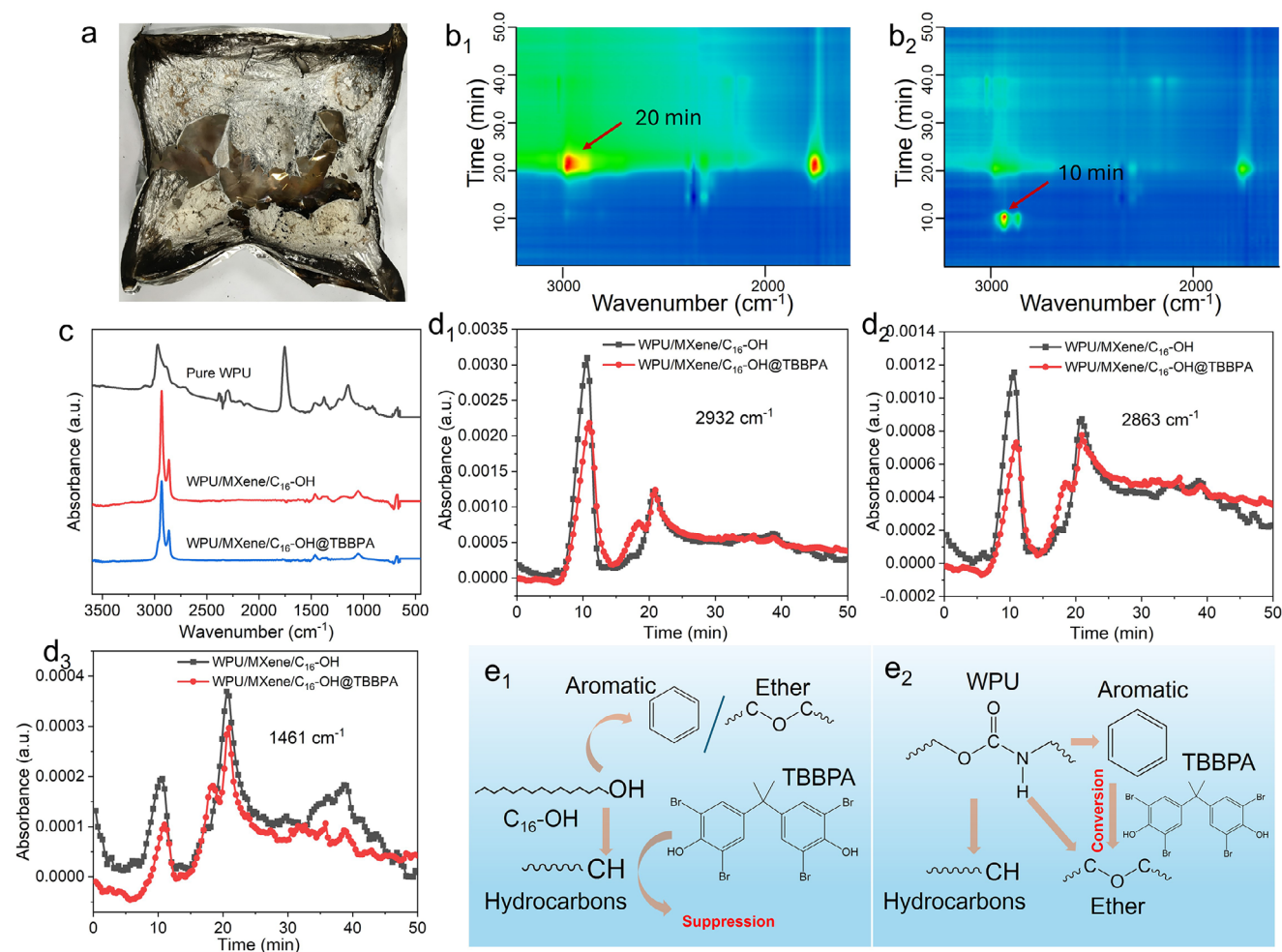


**Figure 6.** (a) Char residue of WPU/MXene/C16-OH@TBBPA after cone calorimeter test. Top view of 3D TG-IR spectra of pure WPU ( $b_1$ ) and WPU/MXene/C<sub>16</sub>-OH ( $b_2$ ); (c) FTIR spectra of pure WPU, WPU/MXene/C<sub>16</sub>-OH, and WPU/MXene/C<sub>16</sub>-OH@TBBPA, corresponding to largest signal intensity; The curves of absorbance intensity of hydrocarbons, corresponding to 2932  $\text{cm}^{-1}$  ( $d_1$ ), 2863  $\text{cm}^{-1}$  ( $d_2$ ), and 1461  $\text{cm}^{-1}$ ; Flame-retardant mechanism of TBBPA to pyrolysis behavior of C<sub>16</sub>-OH ( $e_1$ ) and WPU ( $e_2$ ).

decreased. The above results indicate that the addition of TBBPA effectively decreases the production of hydrocarbons from n-hexadecanol, but not aromatic compounds and ether. The peak intensity of 2932 and 2863  $\text{cm}^{-1}$  near 20 min from WPU pyrolysis isn't influenced by incorporating TBBPA. Even though the peak intensity of 1461  $\text{cm}^{-1}$  near 20 min is further decreased, the opposite phenomenon is presented for 1049  $\text{cm}^{-1}$  (Figure S18, Supporting Information). These results indicate that aromatic compounds from WPU pyrolysis may be converted into ether by the addition of TBBPA. As presented in Figure 6e, TBBPA can suppress hydrocarbon production from the thermal pyrolysis of n-hexadecanol but does not affect the aromatic compounds and ether (Figure 6e<sub>1</sub>). TBBPA does not decrease the hydrocarbon production from WPU resin, but its addition increases the formation of ether compounds by converting aromatic compounds (Figure 6e<sub>2</sub>). Despite TBBPA exhibiting different flame-retardant mechanisms in WPU resin and fatty alcohol, its addition still effectively decreases the heat and toxic gas production of WPU/MXene/C<sub>16</sub>-OH composite film, further enhancing fire safety.

### 3. Conclusion

Herein, we developed a self-adaptive composite film, functioning as a “smart window”, by leveraging the phase change behavior of fatty alcohol, the photo-thermal conversion of MXene nanosheets, and the gaseous flame-retardant effect of TBBPA. This innovative film aims to reduce energy consumption for cooling buildings, provide adequate daylighting, and ensure privacy and safety. The photo-thermal conversion properties of MXene nanosheets cause n-hexadecanol to melt thermally, aligning its refractive index with that of WPU, thereby enabling a transparency switch from 34.4% to 65.0%. The switch temperature can be easily adjusted by varying the composition and types of fatty alcohol. High transparency during the day allows for desirable daylighting, while low transparency at night ensures privacy. Besides, the solar absorption capability of MXene nanosheets prevents direct solar illumination from affecting indoor environments. Field tests confirm a temperature reduction of  $\approx 4.2$  °C when WPU/MXene/C<sub>16</sub>-OH@TBBPA replaces PET film. Furthermore, *EnergyPlus* simulations indicate that using

WPU/MXene/C<sub>16</sub>-OH@TBBPA can significantly reduce energy consumption for cooling buildings, particularly in hot cities and regions. Attributed to its selective solubility, TBBPA dissolves in thermally melted fatty alcohol without affecting the optical performance of the composite films. The gaseous flame-retardant mechanism of TBBPA effectively suppresses hydrocarbon production, thereby reducing the fire hazard associated with this composite film. Cone calorimeter results show that incorporating 2.0 wt.% TBBPA into WPU/MXene/C<sub>16</sub>-OH reduces the peak heat release rate (PHRR) by 16.5%. In summary, with a straightforward processing approach, the designed WPU/MXene/C<sub>16</sub>-OH@TBBPA meets daylighting needs protects privacy at night, and offers enhanced fire safety, providing substantial practical value.

## 4. Experimental Section

**Raw Materials:** Commercial WPU (F0401, 33.3 wt.% mass concentration) was purchased from Jitian Chemical Company. The fatty alcohols, including n-hexadecanol, laurinol, and n-decanol, were provided by Aladdin Industrial Co., Ltd. TBBPA was obtained from the Macklin Industrial Co., Ltd. (China). MXene nanosheets were prepared and provided by the previous research.<sup>[24a]</sup> In addition, organic solvents were not used here and only deionized water was consumed.

**Synthesis of WPU/MXene/C<sub>16</sub>-OH@TBBPA:** First, TBBPA was dissolved in thermal-melting n-hexadecanol at 60 °C, and the solution cooled to form a solid product, accompanied by a mild magnetic stirring. Second, the n-hexadecanol/TBBPA composite was directly added to 30 g WPU suspension with different mass ratios, including 10, 20, 30, 40, and 50 wt.%. Finally, the suspension was heated above the temperature corresponding to the phase change of n-hexadecanol and cooled to room temperature. The formed thick suspension was coated onto the surface of the PTFE mold by a scraper blade of 1.0 mm and further dried at room temperature. The mass ratio of TBBPA to WPU/C<sub>16</sub>-OH was 2.0 wt.%. Other fatty alcohols were also incorporated into WPU resin with the same procedure. Provided by the previous work, MXene nanosheets were added and well dispersed into WPU suspension with sonication of 30 min.<sup>[24a]</sup> The mass ratio of MXene nanosheets to WPU resin was 0.2 wt.%. Similar, the formed WPU/MXene suspension was coated onto the surface of the PTFE mold by a blade method, and further dried at room temperature. The two films were combined tightly by a cold compression under 5 MPa, thus preparing a targeted product, i.e., WPU/MXene/C<sub>16</sub>-OH@TBBPA.

**Characterization:** The fracture structure of the composite film was observed with an XL-30 ESEM scanning electron microscope (SEM) at an acceleration voltage of 20.0 kV. Thermogravimetric analysis (TGA) was executed with a TGA Q5000 IR thermogravimetric analyzer (TA Instruments, U.S.) at a heating rate of 20 °C min<sup>-1</sup>. A combustion test was performed on a cone calorimeter (Fire Testing Technology, UK) according to ISO 5660-1 standard procedure. Each specimen, with a thickness of ≈1.0 mm, was exposed horizontally to 35 kW m<sup>-2</sup> external heat flux. All samples were tested three times. Thermogravimetric analysis-infrared spectrometry (TG-IR) was investigated with a TGA Q5000IR thermogravimetric analyzer linked to a Nicolet 6700 FTIR spectrophotometer from 20 to 700 °C at 10 °C min<sup>-1</sup> (N<sub>2</sub> atmosphere, flow rate of 30 mL min<sup>-1</sup>). The micro-sized combustion behavior of composite films was performed on a microscale combustion calorimeter (MCC-1, FTT). Differential scanning calorimetry (DSC) was conducted using a Q25 instrument (TA, USA) at a heating rate of 5 °C min<sup>-1</sup> from -10 to 60 °C under a nitrogen atmosphere.

**Thermal Management Test:** UV-vis-NIR spectroscopy was performed using a Perkin-Elmer LAMBDA 1050 high-performance UV-vis-NIR double beam spectrophotometer. The emittance spectrum was obtained by measuring reflectance (R) and transmittance (T), which were calculated as 1-R-T. According to Kirchhoff's law, emittance was equivalent to absorptance when an object was in thermodynamic equilibrium. Outdoor

cooling performance was measured using a self-assembled radiant refrigeration performance test device in Hefei, China. A small meteorological station was established to monitor the humidity, temperature, and solar intensity. Meanwhile, a hollow PS foam was used as a supporter, covered by the Al foil. The composite film and its control sample (PET film) cover the surface of PS foam. Four thermocouples were used to record the temperatures, including the surface of two films and the bottom of hollow PS foams. According to Equation (1), the reflectivity in the solar waveband can be calculated. Where r was the reflection (%), λ is the wavelength (nm), λ<sub>min</sub> and λ<sub>max</sub> are the minimum and maximum wavelength, respectively. θ is the polar angle, and φ is the azimuthal angle. I<sub>solar</sub>(λ) is the AM1.5G solar spectral irradiance at λ, and r<sub>solar</sub>(λ) is the light reflection (%) at λ.

$$r(\lambda, \theta, \varphi) = \int_{\lambda_{\min}}^{\lambda_{\max}} I_{\text{solar}}(\lambda, \theta, \varphi) r_{\text{solar}}(\lambda, \theta, \varphi) d\lambda / \int_{\lambda_{\min}}^{\lambda_{\max}} I_{\text{solar}}(\lambda, \theta, \varphi) d\lambda \quad (1)$$

According to Equation (2), the emissivity can be accurately obtained. The ε is the IR emissivity (%), λ is the wavelength (μm), λ<sub>min</sub> and λ<sub>max</sub> are 5 and 15 μm, respectively. θ is the polar angle and φ is the azimuthal angle. I(λ) means the spectral intensity emitted by the blackbody at λ.

$$\varepsilon(\lambda, \theta, \varphi) = \int_{\lambda_{\min}}^{\lambda_{\max}} I(\lambda, \theta, \varphi) \varepsilon(\lambda, \theta, \varphi) d\lambda / \int_{\lambda_{\min}}^{\lambda_{\max}} I(\lambda, \theta, \varphi) d\lambda \quad (2)$$

**EnergyPlus Simulation:** In this simulation, a composite film designed and PET film were used as the windows of buildings. Solar transmittance, solar reflectance, visible transmittance, visible reflectance, and emissivity of PET film were set as 0.9, 0.1, 0.9, 0.1, and 0.84, respectively. The switching temperature of the composite film was different with the environment temperature and provided by the photo-thermal conversion function of MXene under solar intensity. Consequently, the environment temperature of 26 °C was set as the switch temperature. Besides, the thermal conductivity, density, and specific heat capacity of the composite film designed and PET film were set as 0.2 W mK<sup>-1</sup>, 1.0 g cm<sup>-3</sup>, and 1.3 kJ (kg × K)<sup>-1</sup>. The weather and climatic region employ the Koppen's province.

## Supporting Information

Supporting Information is available from the Wiley Online Library or from the author.

## Acknowledgements

The authors acknowledge financial support from the National Natural Science Foundation of China (22205228), the Innovation and Technology Fund (ITP/023/22TP), and PolyU Postdoc Matching Fund (1-W27).

## Conflict of Interest

The authors declare no conflict of interest.

## Data Availability Statement

The data that support the findings of this study are available from the corresponding author upon reasonable request.

## Keywords

fatty alcohol, fire safety, photo-thermal material, smart windows, thermal management

Received: February 6, 2025

Revised: March 24, 2025

Published online: April 3, 2025

- [1] X. Yin, R. Yang, G. Tan, S. Fan, *Science* **2020**, *370*, 786.
- [2] a) S. Tan, S. Guo, Y. Wu, T. Zhang, J. Tang, G. Ji, *Adv. Funct. Mater.* **2024**, *35*, 2415921; b) T. Li, Y. Zhai, S. He, W. Gan, Z. Wei, M. Heidarinejad, D. Dalgo, R. Mi, X. Zhao, J. Song, *Science* **2019**, *364*, 760; c) S. Wang, Z. Xu, T. Wang, T. Xiao, X.-Y. Hu, Y.-Z. Shen, L. Wang, *Nat. Commun.* **2018**, *9*, 1737.
- [3] a) K. Lin, S. Chen, Y. Zeng, T. C. Ho, Y. Zhu, X. Wang, F. Liu, B. Huang, C. Y.-H. Chao, Z. Wang, *Science* **2023**, *382*, 691; b) J. Zhou, T. G. Chen, Y. Tsurimaki, A. Hajj-Ahmad, L. Fan, Y. Peng, R. Xu, Y. Wu, S. Assaworrorarit, S. Fan, *Joule* **2023**, *7*, 2830.
- [4] L. Hu, C. Wang, H. Zhu, Y. Zhou, H. Li, L. Liu, L. Ma, *Small* **2024**, *20*, 2306823.
- [5] a) C. Lin, J. Hur, C. Y. Chao, G. Liu, S. Yao, W. Li, B. Huang, *Sci. Adv.* **2022**, *8*, abn7359; b) D. Yu, S. Zhuo, J. Wang, Z. Liu, J. Ye, Y. Wang, L. Chen, X. Ouyang, K. Q. Zhang, X. Q. Zhou, *Small* **2023**, *19*, 2205833; c) Y. Zhao, S. Tan, J. Yu, R. Yu, T. Xu, J. Zheng, G. Ji, *Adv. Mater.* **2025**, *37*, 2412845.
- [6] a) J. Xu, D. Chen, S. Meng, *Sci. Adv.* **2022**, *8*, add2392; b) S. Wang, T. Jiang, Y. Meng, R. Yang, G. Tan, Y. Long, *Science* **2021**, *374*, 1501; c) S. Chen, Z. Wang, H. Ren, Y. Chen, W. Yan, C. Wang, B. Li, J. Jiang, C. Zou, *Sci. Adv.* **2019**, *5*, aav6815.
- [7] Z. Wen, Y. Ke, C. Feng, S. Fang, M. Sun, X. Liu, Y. Long, *Adv. Mater. Interfaces* **2021**, *8*, 2001606.
- [8] C. Ji, Z. Wu, L. Lu, X. Wu, J. Wang, X. Liu, H. Zhou, Z. Huang, J. Gou, Y. Jiang, *J. Mater. Chem. C* **2018**, *6*, 6502.
- [9] Y. Cui, Y. Ke, C. Liu, Z. Chen, N. Wang, L. Zhang, Y. Zhou, S. Wang, Y. Gao, Y. Long, *Joule* **2018**, *2*, 1707.
- [10] G. Chen, K. Wang, J. Yang, J. Huang, Z. Chen, J. Zheng, J. Wang, H. Yang, S. Li, Y. Miao, *Adv. Mater.* **2023**, *35*, 2211716.
- [11] N. P. Hyslop, *Atmos. Environ.* **2009**, *43*, 182.
- [12] a) R. Li, L. Zhang, L. Shi, P. Wang, *ACS Nano* **2017**, *11*, 3752; b) T. Xu, S. Tan, S. Li, T. Chen, Y. Wu, Y. Hao, C. Liu, G. Ji, *Adv. Funct. Mater.* **2024**, *34*, 2400424.
- [13] W. Niu, G. Y. Chen, H. Xu, X. Liu, J. Sun, *Adv. Mater.* **2022**, *34*, 2108232.
- [14] R. N. Wijesena, N. D. Tissera, V. Rathnayaka, H. Rajapakse, R. M. de Silva, K. N. de Silva, *Carbohydr. Polym.* **2020**, *237*, 116132.
- [15] J. Shi, M. Li, *Sol. Energy* **2020**, *205*, 62.
- [16] E. A. Crespo, L. P. Silva, M. n. A. Martins, L. Fernandez, J. Ortega, O. Ferreira, G. Sadowski, C. Held, S. o. P. Pinho, J. o. A. Coutinho, *Ind. Eng. Chem. Res.* **2017**, *56*, 12192.
- [17] H. N. Kim, S. Yang, *Adv. Funct. Mater.* **2020**, *30*, 1902597.
- [18] K. Lu, L. Hu, M. Delichatsios, F. Tang, Z. Qiu, L. He, *Proc. Combust. Inst.* **2015**, *35*, 2615.
- [19] W. Cai, L. Qi, T. Cui, B. Lin, M. Z. Rahman, X. Hu, Y. Ming, A. P. Chan, W. Xing, D. Y. Wang, *Adv. Funct. Mater.* **2024**, *35*, 2412902.
- [20] a) M. A.-E. Abdallah, *Environ. Int.* **2016**, *94*, 235; b) X. Guan, S. Tan, L. Wang, Y. Zhao, G. Ji, *ACS Nano* **2023**, *17*, 20525.
- [21] A. Patti, D. Acierno, *J. Vinyl Addit. Technol.* **2023**, *29*, 589.
- [22] A. Hongsingthong, T. Krajangsang, I. A. Yunaz, S. Miyajima, M. Konagai, *Appl. Phys. Express* **2010**, *3*, 051102.
- [23] J. Shi, M. Qin, W. Aftab, R. Zou, *Energy Storage Mater.* **2021**, *41*, 321.
- [24] a) W. Cai, Z. Li, T. Cui, X. Feng, L. Song, Y. Hu, X. Wang, *Composites, Part B* **2022**, *244*, 110204; b) T. Cui, W. Cai, Y. Zheng, J. Wang, B. Lin, Z. Gui, J. Zhu, *Chem. Eng. J.* **2023**, *473*, 145357.
- [25] X. Li, R. Wu, Y. Shi, S. Ding, M. Li, S. Xu, B. Zhang, L. Tong, Q. Wang, *Mater. Today Chem.* **2024**, *39*, 102142.
- [26] L. Liang, R. Yu, S. J. H. Ong, Y. Yang, B. Zhang, G. Ji, Z. J. Xu, *ACS Nano* **2023**, *17*, 12409.
- [27] Y. Sun, C. Liu, Y. Hong, R. Liu, X. Zhou, *Prog. Org. Coat.* **2019**, *137*, 105323.
- [28] M. Kumar, M. D. Barbhai, *Emerg. Manag. Sci. Technol* **2023**, *3*, 17.
- [29] Z. Liu, L. Jiang, X. Fu, J. Zhang, J. Lei, *J. Therm. Anal. Calorim.* **2020**, *140*, 2159.
- [30] M. Altarawneh, A. Saeed, M. Al-Harshsheh, B. Z. Dlugogorski, *Prog. Energy Combust. Sci.* **2019**, *70*, 212.
- [31] L. Zheng, J. Zhan, J. Wang, Z. Xu, X. Mu, *Polym. Degrad. Stab.* **2024**, *230*, 111039.
- [32] Y. Luo, R. Jiang, Y. Xu, H. Wang, Z. Qiu, J. Huang, Y. Zheng, *J. Appl. Polym. Sci.* **2025**, *142*, 56481.
- [33] W. Chen, P. Liu, Y. Liu, Z. Liu, *Chem. Eng. J.* **2022**, *446*, 137239.
- [34] W. Cai, Z. Li, H. Xie, W. Wang, T. Cui, B. Lin, L. Qi, X. Hu, Y. Du, Y. Ming, *Chem. Eng. J.* **2024**, *483*, 149006.
- [35] S. Xu, E. Liu, R. Gao, H. Du, Z. Chen, Q. Sun, Z. Xu, *J. Anal. Appl. Pyrolysis* **2024**, *177*, 106301.
- [36] F. Juliá, T. Constantin, D. Leonori, *Chem. Rev.* **2021**, *122*, 2292.
- [37] B. Yuan, S. Wu, H. Zhao, Y. Niu, Z. Gao, Y. Zhu, Y. Kong, H. Jin, P. Wang, *J. Therm. Anal. Calorim.* **2024**, *149*, 8027.